Increasing arsenic immobilization capacity of a binder prepared by arsenic-containing biohydrometallurgy waste

Effects of ferric/ferrous salts addition

Zhao, Yingliang; Sun, Yong; Guo, Zhenbang; Sun, Xiaogang; Qiu, Jingping

DOI
10.1016/j.jece.2023.110206

Publication date
2023

Document Version
Final published version

Published in
Journal of Environmental Chemical Engineering

Citation (APA)
Zhao, Y., Sun, Y., Guo, Z., Sun, X., & Qiu, J. (2023). Increasing arsenic immobilization capacity of a binder prepared by arsenic-containing biohydrometallurgy waste: Effects of ferric/ferrous salts addition. *Journal of Environmental Chemical Engineering*, *11*(3), Article 110206. https://doi.org/10.1016/j.jece.2023.110206

Journal of Environmental Chemical Engineering 11 (2023) 110206

Contents lists available at ScienceDirect

Journal of Environmental Chemical Engineering

journal homepage: www.elsevier.com/locate/jece

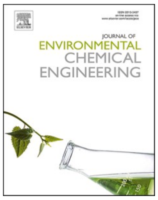

Increasing arsenic immobilization capacity of a binder prepared by arsenic-containing biohydrometallurgy waste: Effects of ferric/ferrous salts addition

Yingliang Zhao [a,b], Yong Sun [a], Zhenbang Guo [a,c], Xiaogang Sun [a], Jingping Qiu [a,*]

[a] *College of Resources and Civil Engineering, Northeastern University, Shenyang, China*
[b] *Department of Civil and Environmental Engineering, The Hong Kong Polytechnic University, Kowloon, Hong Kong*
[c] *Faculty of Civil Engineering and Geosciences, Department of Hydraulic Engineering, Delft University of Technology, Delft, the Netherlands*

ARTICLE INFO

Editor: Apostolos Giannis

Keywords:
Biohydrometallurgy waste
As immobilization
Chemical additives
Density function theory

ABSTRACT

The aim of this study was to improve the immobilization capacity of a binder prepared from As-containing biohydrometallurgy waste (BAW) on arsenic (As) by modifying it with ferric/ferrous salts. The study investigated the chemical fractions of As and its leaching characteristics. Results indicated that the addition of ferric/ferrous salts significantly reduced the mid acido-soluble fraction of As, resulting in decreased As leaching. Among the four ferric/ferrous salts studied, ferrous sulfate (FeS2) performed the best, with only 0.5 wt% of FeS2 achieving satisfactory results. The influence of ferric/ferrous salts on the strength development and reaction products were also investigated. Although the incorporation of ferric/ferrous salts reduced As leaching, it also decreased the early age compressive strength of BAW. Ferric salts had a more significant impact on the strength evolution. In addition, the mechanism of Fe species on As stability using density function theory calculation was explored. Results suggested that As species could be adsorbed on the surface of Fe species through strong covalent bonds. Overall, the study demonstrated that modifying BAW using ferric/ferrous salts could effectively reduce As leaching. However, the decrease in strength especially at the early ages must be taken into consideration when using this method.

1. Introduction

Arsenic (As) has been identified by the World Health Organization as a human carcinogen and is often found in association with other non-ferrous metals such as lead, zinc, nickel, tin, and cobalt. In As-containing ores, valuable elements typically exist in the form of micro-scale inclusions combined with the crystal structure of As-bearing minerals, resulting in lower recovery rates [1]. Therefore, pre-treatment is generally required for the extraction of valuable elements in some As-containing ores [2]. The biohydrometallurgy method is the most commonly used method for treating As-containing ores, which was first used in the 1950 s [3–5]. Microorganisms act as catalysts in this process. Arsenic is dissolved and released into the solution during this process [6]. The ores pretreated with biohydrometallurgy can be further processed using cyanide or other methods. However, the treatment of As-containing ores through biohydrometallurgy produces a large amount of As-containing acidic wastewater (AAW), which can cause serious environmental pollution [7].

In addition, during the pyrometallurgical smelting process of non-ferrous metals (such as copper, nickel, lead, zinc, tin, etc.), some As elements enter into the sulfur dioxide flue gas in the form of smoke, and are then removed by gravity dust collection or electrostatic dust collection; another part of the As is removed through the washing and purification of the flue gas before the acid production of the flue gas, which leads to As entering into the washing wastewater, eventually forming a large amount of AAW. According to statistics, China

---

Abbreviation: BAW, A binder prepared from As-containing biohydrometallurgy waste; AS, Aluminum sulfate; AAW, As-containing acidic wastewater; AW, As-containing biohydrometallurgy waste; BFS, Blast furnace slag; CS, Carbide slag; CFL, Cumulative leaching fraction; D_e, Diffusion coefficient; DFT, Density function theory; DOS, Density of states; FeC3, Ferric chloride; FeS3, Ferric sulfate; FeC2, Ferrous chloride; FeS2, Ferrous sulfate; IR, Immobilization ratio; ICP-OES, Inductively coupled plasma optical emission spectrometer; LI, Leaching index; OPC, Ordinary Portland cement; PDOS, Partial density of states; TCLP, Toxicity characteristic leaching procedure; TG, Thermogravimetric; XRD, X-ray Diffraction.

* Corresponding author.
E-mail address: qiujingping@mail.neu.edu.cn (J. Qiu).

https://doi.org/10.1016/j.jece.2023.110206
Received 10 April 2023; Received in revised form 15 May 2023; Accepted 25 May 2023

Table 1
Chemical composition of the raw materials (wt%).

Materials	CaO	MgO	SiO_2	Al_2O_3	Fe_2O_3	SO_3	K_2O	As_2O_3
AW	28.34	1.90	3.61	1.14	12.76	15.53	0.33	1.48
BFS	38.71	8.90	29.92	16.62	0.37	0.85	0.32	/
CS	95.12	0.38	2.73	0.91	0.60	0.04	0.13	/
OPC	57.20	4.79	21.65	5.84	1.77	0.79	0.09	/

discharges as much as 12 million cubic meters of AAW each year from copper smelting alone [8].

Due to the strong acidity (H_2SO_4 content can reach 10–80 g/L) and high As content (4–30 g/L) of AAW [9], it cannot be discharged or directly utilized. Therefore, the treatment of AAW has aroused worldwide attention. Due to its simplicity and low cost, the most widely used method for industrial treatment of AAW is lime/calcite-ferrate process [10]. The main reagents used in neutralization precipitation are limestone or lime, and the residue after neutralization is mainly treated by stacking after pressure filtration, which leads to the generation of a large amount of As-containing biohydrometallurgy waste (AW) [11]. Statistics show that when treating 1 m^3 of AAW using the lime/calcite-ferrate method, about 70 kg of AW will be produced [12]. Due to the instability of AW, As is easily leached out, causing secondary pollution [13]. Therefore, the safe and rational disposal of AW has attracted widespread attention.

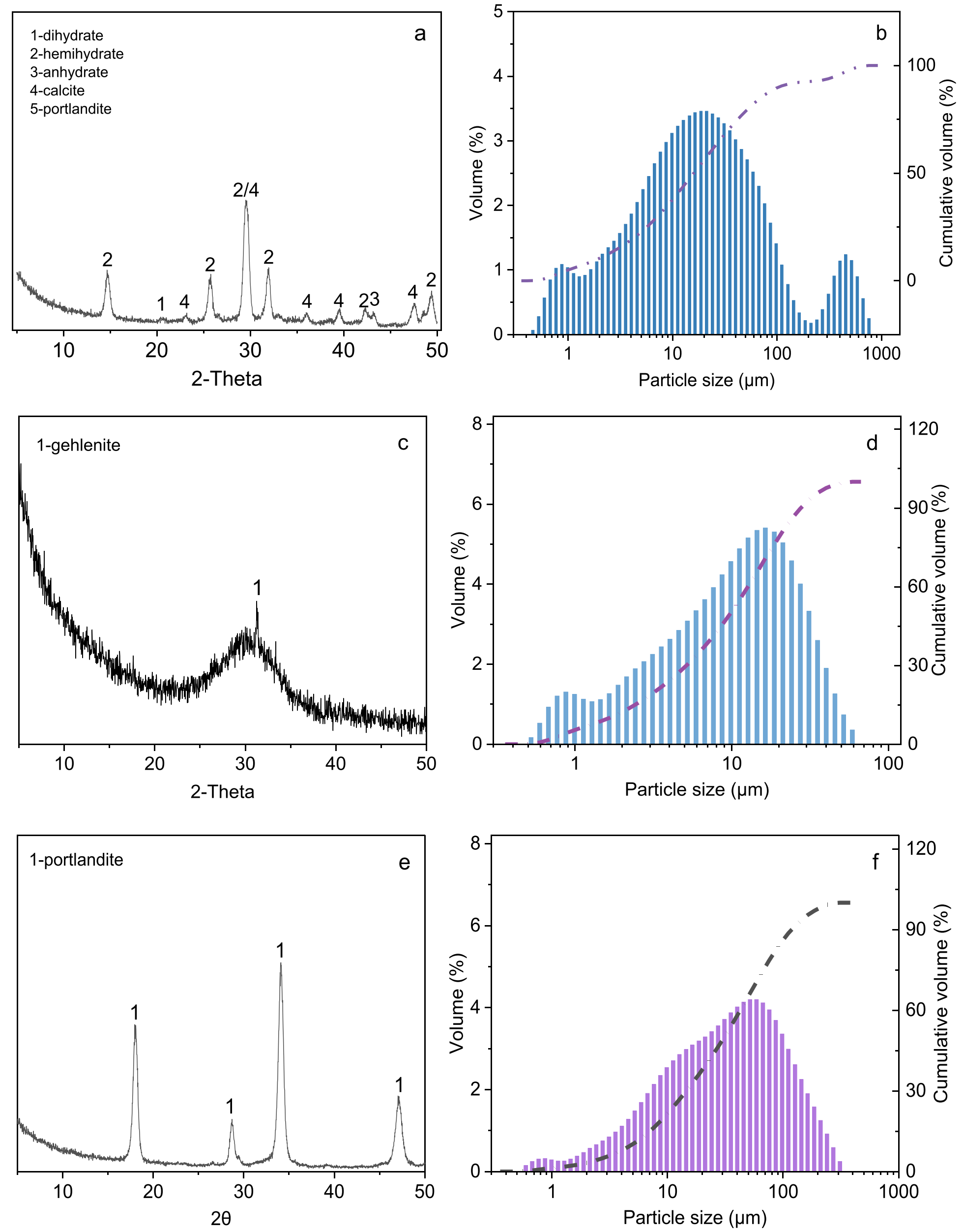

Fig. 1. XRD patterns for As-containing biohydrometallurgy waste (a), blast furnace slag (c) and carbide slag (e), particle size distribution for As-containing biohydrometallurgy waste (b), blast furnace slag (d) and carbide slag (f).

Currently, the main methods for the treatment of AW include solidification using cement [14], stabilization using nano-materials [10], hydrothermal treatment [15], preparation of gypsum[16], and soil amendments [17]. Although these treatment methods can reduce the harm of AW to a certain extent, they generally have drawbacks such as low utilization rate, high treatment cost, and poor volume reduction effect. Treating hazardous materials by cementitous materials is another feasible strategy to reduce their harm to the environment; the hazardous materials commonly mixed with a binder and formed a hard matrix, which could limit the hazardous elements leaching [18,19]. Bah et al. immobilized As using fly ash and mine tailings-based geopolymers, and the results showed that calcite and calcium silicate hydroxide contributed to immobilizing As^V[20]; the geopolymers could be further used as construction materials after arsenic immobilizing [20]. The influence of Si/Al molar ration on the As immobilization effects was investigated by Tian et al., and the percentages of As leaching increased with the increase of the Si/Al ratio [21]. If AW could be used as a raw material for binder production, it is expected to realize 'self-immobilization' effects. Because of its high concentration of calcium sulfate, AW has the potential to be utilized in the production of super sulfated cement (SSC), which is viewed as a viable substitute for OPC because of its economical and eco-friendly attributes [22]. In previous research, we successfully prepared a binder using AW as the main raw material [23–25]. Duo to the As containing characteristics, the immobilization capacity of As in the prepared binder is a crucial consideration. Generally, the immobilization effects of a binder for hazardous elements are related to both physical and chemical parameters. The physical aspects refer to encapsulation of hazardous elements into a compact structure. The solidified cementitious materials are more compact, with reduced permeability, thereby inhibiting the diffusion of hazardous elements [26]. On the chemical side, hazardous elements can react with the components in cementitious materials to produce relatively insoluble, low-toxicity substances [27,28]. For example, studies have shown that Cr(VI) can react with Ca^{2+} in the cementitious reaction system to form calcium chromate precipitation, thereby reducing its leaching concentration [29]. On the other hand, the gels produced during the binders reaction can have a chemical stabilizing effect on hazardous elements (surface adsorption and/or ion substitution). The amount of reaction gels generated during the reaction can also directly affect the physical encapsulation effect of the solidified matrix on hazardous elements.

It has been reported that iron (Fe) species has strong immobilization capacity to As [30,31]. Currently, different types of solid wastes containing As have been effectively immobilized using Fe salts. These solid wastes include arsenic-alkali residue, non-ferrous metal tailings, and red mud [32–34]. Several studies have shown that the primary mechanism of stabilization involves the adsorption and co-precipitation of As by iron (hydr)oxides [35]. Sun et al. [10] treated AW by combining the addition of nano zero valent iron (nZVI) with hydrothermal treatment. As was immobilized in the form of hexagonal arsenic calcium. Under optimal conditions (nZVI dosage of 0.1 g/g of AW, hydrothermal treatment at 150 °C for 12 h), the leaching concentration of As decreased from 22.4 mg/L to 0.015 mg/L.

Inspired by previous research, we optimized and modified the stability of As in BAW by using ferric/ferrous salts. However, unlike previous studies, the addition of ferric/ferrous salts not only changes the chemical fractions of As in BAW but also interferes with the hydration reaction of BAW, thereby affecting the As immobilization capacity of BAW. Therefore, we believe that it is necessary to conduct in-depth research on this issue. In the present work, four ferric/ferrous salts were used to modify the immobilization effects of BAW on As. The chemical fraction of As and its leaching characteristics were studied via TCLP and semi-dynamic leaching. At the same time, the influence of ferric/ferrous salts on the strength development and reaction products was also investigated. Additionally, the mechanism of Fe species on As stability was explored via density function theory (DFT) calculation.

2. Materials and methods

2.1. Materials

The raw materials used in this experiment included As-containing biohydrometallurgy waste (AW), blast furnace slag (BFS), ordinary Portland cement (OPC), carbide slag (CS), aluminum sulfate (AlS), ferrous sulfate ($FeSO_4 \cdot 7\ H_2O$, FeS2), ferric sulfate ($Fe_2(SO_4)_3 \cdot 5\ H_2O$,

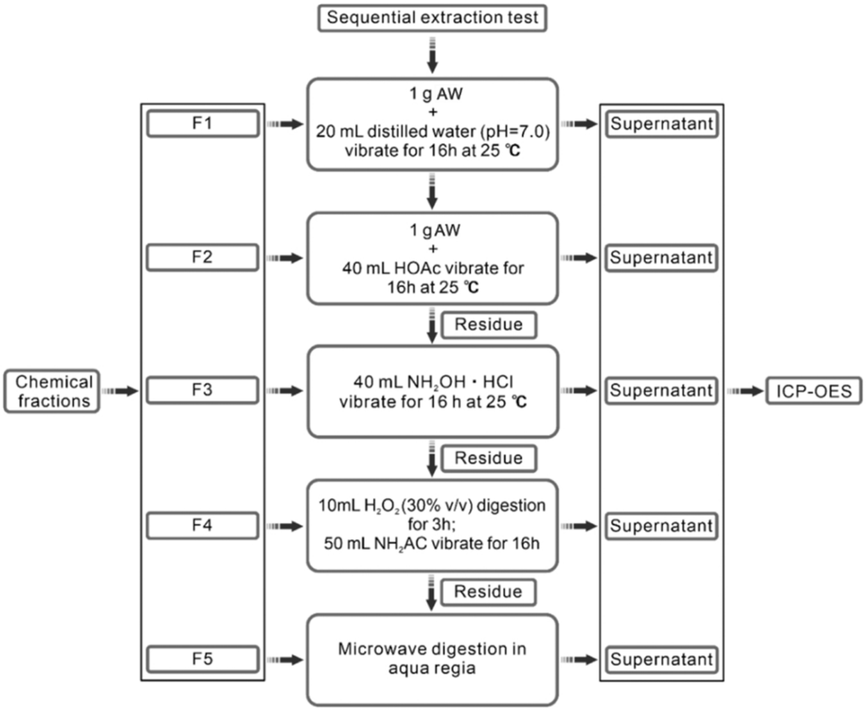

Fig. 2. Sequential extraction test.

FeS3), ferrous chloride ($FeCl_2 \cdot 4\ H_2O$, FeC2) and ferric chloride ($FeCl_3$, FeC3). All test reagents were purchased from Sinopharm Group Chemical Reagent Co., LTD., and they were analytical reagents.

AW was collected from a gold mine located at Fecheng, China, and its chemical composition of AW was shown in Table 1. As can be seen from Table 1, its chemical components were mainly CaO, SO_3 and Fe_2O_3, accounting for more than 76 wt% of the total. CaO had the highest content of about 28 wt%, mainly due to the addition of calcite/quick lime to neutralize the acidity of As-containing acidic wastewater. In addition, the content of As_2O_3 in AW was as high as 1.48 wt%, which was easy to leach and cause environmental pollution.

The phase composition of AW was shown in Fig. 1a. The main phase was hemihydrate, followed by a small amount of dihydrate and anhydrate, which were produced as a result of chemical reactions during the treatment of AAW, as shown in Eq. (1)~(3) [36].

$$\begin{aligned} Fe_2(SO_4)_3 + H_3AsO_4 + CaCO_3 + H_2O = FeOOH + CaSO_4 \\ + FeAsO_4 + 2H_2SO_4 + CO_2\# \end{aligned} \tag{1}$$

$$H_2SO_4 + CaCO_3 = CaSO_4 + CO_2 + H_2O\# \tag{2}$$

$$H_2SO_4 + Ca(OH)_2 = CaSO_4 + 2H_2O\# \tag{3}$$

BFS was provided by Shandong Panlongshan Material Co., LTD and its chemical composition was shown in Table 1. Fig. 1c shows the phase composition of BFS, which consisted mainly of an amorphous phase with only a small amount of gehlenite. The particle size distribution curve of BFS was shown in Fig. 1d, with d10, d50 and d90 values of 1.88 μm, 11.20 μm and 31.30 μm, respectively. Additionally, the specific surface area of BFS was about 435 m^2/kg. Cement was produced by CR Cement Co., LTD., and its chemical components were shown in Table 1.

CS was provided by Xinyu Material Company of Lingshou County, and its chemical components were shown in Table 1, which shows that CS was mainly composed of CaO, with a content exceeding 95 wt%. The phase composition and particle size distribution of CS were shown in Fig. 1e and f. According to Fig. 1e, portlandite was the main component in CS. Besides, the content of particles smaller than 74 μm in CS was about 78% (Fig. 1f).

2.2. Methods

2.2.1. Sample preparation

The mix proportion for the preparation of binder prepared from AW (BAW) were shown in Table S1. The raw materials were dry mixed for 2 min and then water was added to the mixture. The slurry was blended for an additional 5 min to ensure even mixing. A portion of the slurry was injected into a cylindrical mold (50 mm × 100 mm) while the rest was injected into a centrifugal tube (5 mL).

The samples were then placed in a curing box and cured at 20 ± 1 °C and 95% relative humidity until they reached the predetermined ages. The 50 mm × 100 mm cylindrical specimens were mainly used to test the uniaxial compressive strength and leaching characteristics of As, while the samples in the 5 mL centrifugal tube were used to test the phase composition and microstructure.

2.2.2. Sequential extraction procedure

The chemical fractions of As were determined by the sequential extraction procedure according to the methods in GBT 25282–2010. The test procedure was shown in Fig. 2.

2.2.3. Toxicity characteristic leaching procedure

The total amount of harmful elements in the sample was determined by HNO_3-HF-HCl digestion method. 0.2 g sample was mixed with 6 mL HNO_3, 2 mL HCl and 2 mL HF, then the mixed solution was placed in a microwave digestion instrument for digestion at 140 ℃. After cooling, the solution was filtered using a 0.45 μm membrane filter, and inductively coupled plasma optical emission spectrometer (ICP-OES) was used to measure the element concentration.

Toxicity characteristic leaching procedure (TCLP) was conducted according to the methods in GB HJT 300–2007. 10 g ± 0.1 g sample was mixed with 200 mL acetic acid solution ($pH = 2.64 \pm 0.05$) in a 1 L conical flask. The mixture was shocked for 18 h at 23 ± 3 ℃ using a horizontal oscillator. After that, the solution was filtered by 0.45 μm membrane filter to determine the content of As in the filtrate using ICP-OES.

The immobilization ratio (IR) could be calculated according to Eq. (4).

$$IR = \left(1 - \frac{CV}{M}\right) \times 100\%\# \tag{4}$$

where, C was the concentration of As in the leaching solution, mg/L.

V was the volume of the leaching solution, L.

M was the total amount of As in the sample, mg.

2.2.4. Semi-dynamic leaching

Semi-dynamic leaching test was performed according to the methods by Irisawa [37]. The sample (3 cm ϕ × 3 cm H, cured after 28 d, with a surface area of about 42 cm^2) was hanged at the center of the solution using a nylon cord to ensure full contact. Distilled water (about 420 mL) was used as the extraction solution and the test was conducted at 20 ± 1 °C. The leaching solution was collected at 2 h, 7 h, 1d, 2d, 3d, 4d, 14d, 28d, 43d and 91d, and then measured the As concentration.

The diffusion coefficient (D_e, cm^2/s) was obtained using Eqs. (2) and (3) [37].

$$CFL = \frac{2S}{V}\sqrt{\frac{D_e t}{\pi}}\# \tag{5}$$

$$D_e = \frac{\pi}{4}\left(\frac{V}{S}\right)^2 \frac{CFL^2}{t}\# \tag{6}$$

where, V was the samples volume, m^3.

S was the samples' surface area, m^2.

t was the leaching duration, s.

The leachability index (LI) could be calculated from the cumulative D_e, as shown in Eq. (4) [38].

$$LI = \left(\frac{1}{m}\right)\sum_{n=1}^{n=m}\left(-\lg(D_e)\right)_n\# \tag{7}$$

where, n was number of leaching cycles, n = 1–10.

m was the total leaching cycle, m= 10.

By analyzing the *lg(Mt)-lg(t)* diagram's slope, it is possible to determine the leaching mechanism of As, as shown in Eq. (5).

$$\lg(M_t) = \frac{1}{2}\lg(t) + log\left(Q_0 d\sqrt{\frac{D_e}{\pi}}\right)\# \tag{8}$$

where, M_t was the cumulative As release, mg/m^2.

Q_0 was the total amount of As in the sample, mg/kg.

d was the volume density of sample, kg/m^3.

2.2.5. Hydration products

After curing for a certain age, the sample was cut to slices of < 3 mm. They were then mixed with isopropyl alcohol (AR, 99.5%) at a volume ratio of 1:10 and soaked for 24 h to terminate the hydration of the sample [39–41]. After vacuum filtration, the samples were placed in a vacuum drying oven at 45 °C and dried to a constant weight. The dried sample was ground in a mortar to < 74 μm.

The phase composition of the sample was tested by X-Ray Diffraction (XRD, Shimadzu 7000) using a scanning range of 5–90° 2θ with a scanning velocity of 2°/min.

The thermogravimetric (TG) test of the samples was carried out by

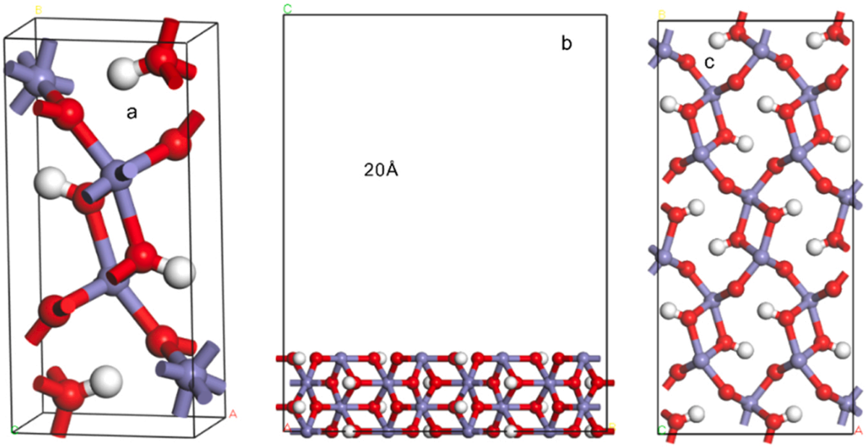

Fig. 3. Crystal structure of FeOOH (a) and FeOOH (001) (b, c), where (c) is top view.

the STA409PC thermal analyzer. About 20 mg samples were put into an alumina crucible and heated from room temperature to 30 °C at a heating rate of 5 °C/min under nitrogen atmosphere. After holding for 30 min, the samples were heated to 1000 °C at a heating rate of 15 °C/min to obtain the TG/DTG curve of the samples.

2.2.6. *Compressive strength*

The compressive strength of the sample was tested after curing for a certain age. After the sample was removed from the curing box, the upper and lower surfaces were polished smooth for good contact with the press. The compressive strength was tested by Humboldt HM-5030 press with a pressure loading speed of 1 mm/min. Five specimens were repeatedly tested for each proportion of samples, and the average value was taken as the final compressive strength of the sample.

2.2.7. *Pore structure*

The pore size distribution was measured by Micromeritics' AutoPore IV 9500 according to ASTM D4404–18. The maximum working pressure was 414 MPa and the pore size was measured in the range of 3–1000 µm. Before testing, 1 × 1 × 1 cm^3 pieces were soaked in isopropyl alcohol for 3 days and dried in a vacuum drying box at 40 °C for 24 h.

2.2.8. *Density function theory calculations*

The model of FeOOH was used in the present work, as shown in Fig. 3a, and the cell parameters before and after geometric optimization are shown in Table S2. (001) surface is generally considered as a natural cleavage surface [42], and its surface contains a large amount of unsaturated Fe, which is conducive to the occurrence of adsorption. Therefore, FeOOH (001) surface was selected for calculation in this simulation, and a 20 Å vacuum layer was added on its surface along the

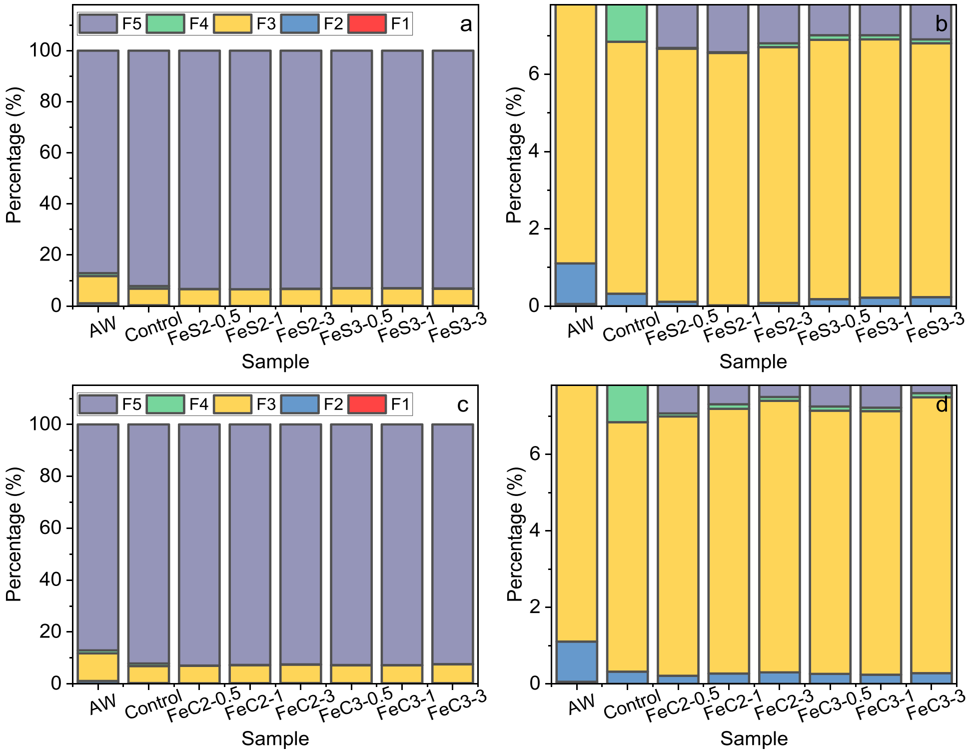

Fig. 4. Influence of ferric/ferrous salt on the chemical fraction of As in BAW: water-soluble fraction (F1), mid acido-soluble fraction (F2), reducible fraction (F3), oxidizable fraction (F4), residual fraction (F5).

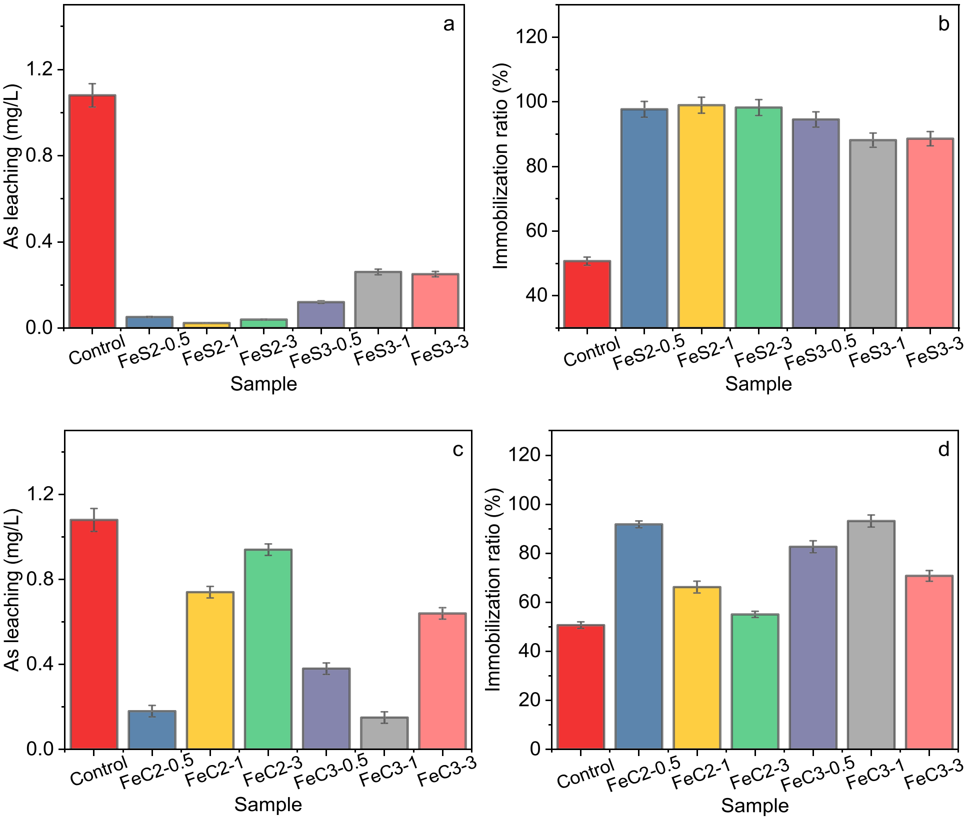

Fig. 5. Influence of ferric/ferrous salt on the leaching concentration of As (a, c) and the immobilization ratio (b, d).

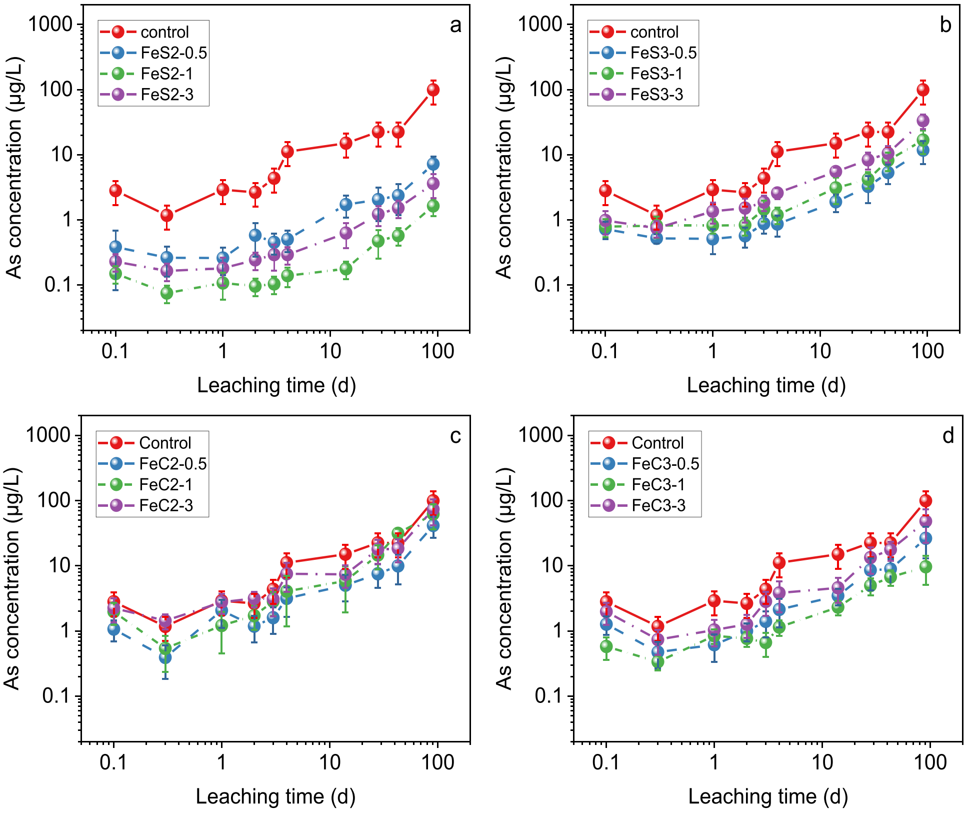

Fig. 6. The influence of ferric/ferrous salt on the As leaching concentration from BAW.

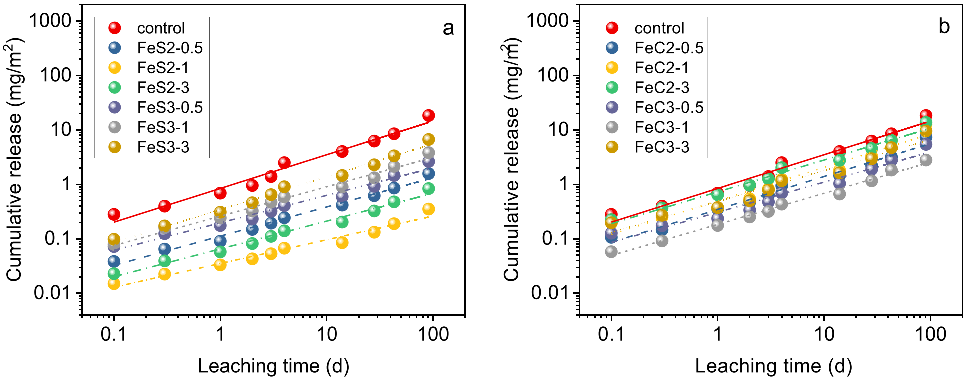

Fig. 7. The influence of ferric/ferrous salt on the cumulative mass release of As from BAW.

c-axis, as shown in Fig. 3b and c. The final model size used for calculation was 9.16 Å × 19.42 Å × 25 Å. In addition, Na$^+$ was added to the system to balance the charge when simulating the interaction of AsO_4^{3-}/AsO_3^{3-} with FeOOH (001) surface.

(Note: red, blue grey and white atoms refer to O, Fe and H).

The DFT calculation was performed using the CASTEP module in Materials studio 8.0 (Accelrys Inc.). The exchange functional uses PBE-GBA [43]. The BFGS algorithm was used to optimize the atomic position [44]. The interaction between electrons was described by ultra-soft pseudopotential [44]. The convergence thresholds for interatomic force, internal stress and atomic displacement were set at 0.03 eV•A^{-1}, 0.05 GPa and 0.001 A, respectively. The convergence threshold of the total energy change and the self-consistent iteration accuracy were set as 1.0×10^{-5} eV•atom^{-1} and 1.0×10^{-6} eV• atom^{-1}, respectively. Based on the convergence test, the cut off energy used in the calculation was 400 eV. In the calculation of FeOOH cell geometry optimization, 5 × 3 × 9 was used for sampling in Brillouin region, while in the calculation of FeOOH (001), Γ point was used to balance calculation amount and efficiency.

3. Results and discussion

3.1. Sequential extraction procedure

The addition of FeS2 and FeS3 to BAW had an impact on the chemical fractions of As, as shown in Fig. 4a and b. Compared to the control sample, both FeS2 and FeS3 reduced the content of F2, with FeS2 showing better results. Fig. 4b demonstrates that the content of F2 decreased as the dosage of FeS2 increased, while FeS3 had no significant effect. This change in chemical fractions was mainly due to the addition of Fe species forming a stable Fe-As complex, reducing the activity of As [45].

The effects of FeC2 and FeC3 on the chemical fractions of As in BAW were less significant than those of FeS2 and FeS3, as shown in Fig. 4c and d. Adding ferric/ferrous salts interfered with the hydration reaction process of the cementing material, affecting the type and amount of reaction products, which ultimately influenced the chemical fractions of As.

3.2. Leaching characteristics

The effect of FeS2 and FeS3 on the immobilization effects of As in BAW was investigated via TCLP and the results were presented in Fig. 5a and b. The As leaching amounts in BAW were found to be 0.051 mg/L, 0.023 mg/L, and 0.039 mg/L at the content of FeS2 of 0.5 wt%, 1 wt%, and 3 wt%, respectively, with corresponding As immobilization rates of 97.67%, 98.95%, and 98.22%. The immobilization rates of FeS3 on As in BAW were slightly weaker, consistent with the results of chemical fractions of As in Fig. 4a and b.

Previous studies have demonstrated the excellent immobilization capacity of Fe species for As [30]. In BAW, As mainly existed in the form of Ca-As, S-As, and Fe-As complexes. Due to the presence of a large amount of Ca in the reaction system, the free As combined with Ca to produce more Ca-As complexes, which had low stability and was easily leached during the TCLP test. FeS2 acted as an oxidant to disrupt the Ca/S-As complex and promoted the transformation of unstable Ca-As and S-As complexes to more stable Fe-As complexes, enhancing the immobilization capacity of As. However, the effect of FeS3 on the immobilization capacity of As was not as good as that of FeS2, likely due to its weak ability to promote the transformation of Ca/S-As complex to Fe-As complex through the co-precipitation of As by iron (hydr)oxides [46]. Higher ferric/ferrous salt content, such as 3 wt%, did not produce better results than the lower content, possibly due to the incorporation of excess SO_4^{2-}, resulting in the formation of excessive ettringite gel and

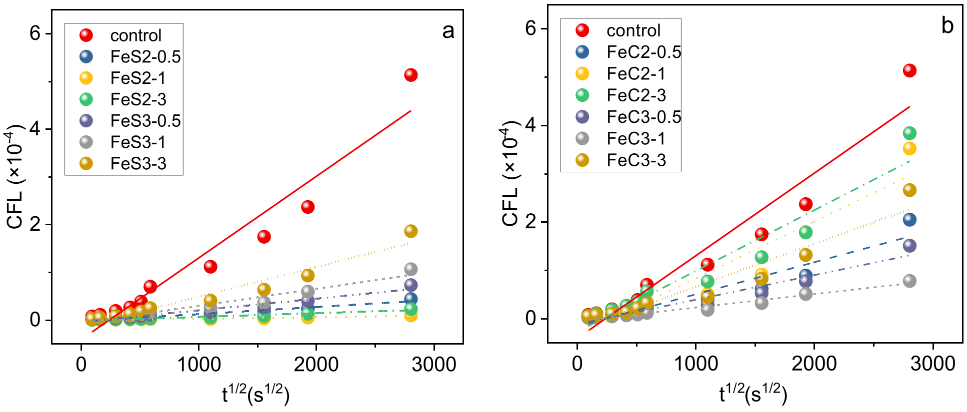

Fig. 8. The plot of $t^{1/2}$-*CFL* : influence by FeS2 and FeS3 (a), FeC2 and FeC3 (b).

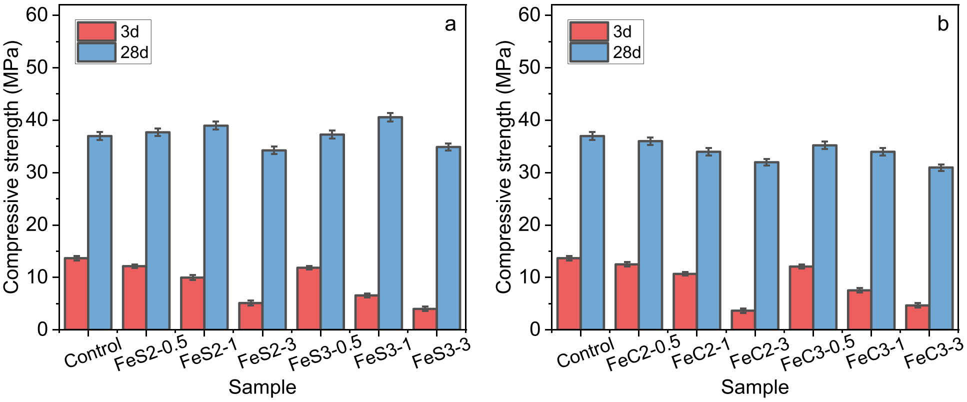

Fig. 9. Influence of ferric/ferrous salt on the compressive strength of BAW samples: (a) sulfate, (b) chloride.

causing damaging expansion of BAW.

Fig. 6 showed that the addition of ferric/ferrous salt did not change the leaching characteristics of As over time, which showed an increasing trend with the leaching time. However, the addition of ferric/ferrous salt reduced the leaching concentration of As. The main reason was that the incorporation of ferric/ferrous salt changed the chemical fractions of As and improved its stability. Fig. 6 also showed that FeS2 had the most significant reduction in As leaching, while FeC2 had the least effect. The *lg(Mt)-lg(t)* curves (Fig. 7) showed a linear relationship between M_t and t, with fitting results (Mt, slope, and R^2) presented in Table S3.

Table S3 presents the relationship between the content of ferric/ferrous salt and the total amount of As leaching. The results indicate that there is no absolute linear relationship between them, which is consistent with the results of TCLP. This is because the synergistic effect of ferric/ferrous salt on the immobilization effect of As and the intervention of BAW hydration reaction creates a certain dynamic balance between them. When the dosage of FeS2 was 0.5 wt%, 1 wt% and 3 wt%, the total amount of As leaching in the sample was 1.57 mg/m^2, 0.35 mg/m^2, and 0.84 mg/m^2, respectively. The reduction in the total amount of As leaching was 91.44%, 98.09%, and 95.42%, respectively, compared with the control sample. The optimal dosage was found to be 1 wt%.

However, the total leaching amount of As in the sample increased with the dosage of FeS3. The optimal effect was achieved when the dosage of FeS3 was 0.5 wt%, and the total leaching amount of As was 2.62 mg/m^2, which was about 85.71% lower than that of the control sample. This suggests that the effect of FeS2 on the immobilization effect of As was better than that of FeS3. Additionally, FeC2/FeC3 was less effective at immobilizing As than FeS2/FeS3. The optimal dosage of FeC2 and FeC3 was 0.5 wt% and 1 wt%, respectively. The total amount of As leaching was 7.32 mg/m^2 and 5.40 mg/m^2, respectively, which was about 60.09% and 84.79% lower than that of the control sample. This phenomenon was likely due to the effect of FeC2/FeC3 on BAW reaction.

Fig. 8 shows the diagram of CFL-$t^{\frac{1}{2}}$, which illustrates the linear relationship between CFL and $t^{\frac{1}{2}}$. The fitting parameters were listed in Table S4. Eqs. (3) and (4) were used to calculate the diffusion coefficient (D_e) of As, and the results were presented in Table S4. The As diffusion coefficient of BAW samples after being modified by ferric/ferrous salt ranged from 10^{-15} to 10^{-18} cm^2/s, which were reduced compared to the control samples. The addition of 1 wt% FeS2 resulted in the lowest diffusion coefficient, about 2.42×10^{-18} cm^2/s. The lower the diffusion coefficient, the weaker the activity of As, indicating that BAW samples showed optimal immobilization capacity for As after the incorporation of 1 wt% FeS2.

Eq. (5) was used to calculate the As leaching index (*LI*) in the sample, and the results were shown in Table S4. The leaching index of all samples was less than 9, which was effective for As immobilization [38]. The maximum leaching index was found in sample FeS2–1, about 17.73, which increased by more than 20% compared with the control sample.

3.3. Compressive strength

Fig. 9 shows the effect of ferric/ferrous salt on the compressive strength development of BAW. Specifically, Fig. 9a displays the impact of FeS2 and FeS3 on the compressive strength of BAW samples. Generally, the addition of FeS2 and FeS3 reduced the early compressive strength of BAW, with the reduction increasing as the dosage of FeS2/FeS3 increased. As shown in Fig. 9a, the addition of 0.5 wt%, 1 wt%, and 3 wt% FeS2 resulted in a reduction of about 11.12%, 27.06%, and 62.55%, respectively, in the 3d compressive strength of BAW. Similarly, the 3d compressive strength of BAW decreased by 13.31%, 51.87%, and 70.81% at 0.5 wt%, 1 wt%, and 3 wt% FeS3, respectively.

The reduction in the early compressive strength of BAW due to the inclusion of FeS2/FeS3 can be attributed to the introduction of SO_4^{2-} ions. While these ions contribute to the formation of ettringite, their precipitation at the early stages leads to the formation of a dense coating on the BFS surface. This coating inhibits the further dissolution and reaction of BFS, which results in a significant reduction in the amount of reaction products produced.

The inhibitory effect of FeS3 on early compressive strength was more evident, as it reacts easily with H_3AsO_4 and CaCO3 in the reaction system, producing H_2SO_4 and CO_2 in the products (Eq. 10). The formation of H_2SO_4 reduced the pH value of the reaction system, which inhibited the progress of the reaction, reduced the formation of early reaction products, and lowers the early strength of BAW.

$$Fe_2(SO_4)_3 + H_3AsO_4 + CaCO_3 + 2H_2O = Fe(OH)_3 + CaSO_4 \\ + FeAsO_4 + 2H_2SO_4 + CO_2\# \tag{9}$$

After curing for 28 days, as shown in Fig. 9a, it was observed that the addition of FeS2/FeS3 in amounts less than 3 wt% increased the 28-day compressive strength of BAW. This increase resulted from the supply of a certain amount of additional SO_4^{2-} ions, which promoted the formation of ettringite in the long run. However, the 28d compressive strength of BAW decreased when the content of FeS2/FeS3 exceeded 3 wt%. The addition of too many SO_4^{2-} ions was likely to generate too much ettringite in the reaction system, leading to destructive expansion and reduced compressive strength.

Excessive FeS3 generated a large amount of CO_2 in the reaction system, resulting in high porosity of BAW samples and reducing their compressive strength. High porosity, especially open porosity, reduced the compressive strength of the sample and increased the leaching of harmful elements from the system. This explains why the As immobilization rate of BAW modified with FeS3 was lower than that of samples added with FeS2.

Fig. 9b displays the effect of FeC2/FeC3 on the evolution of

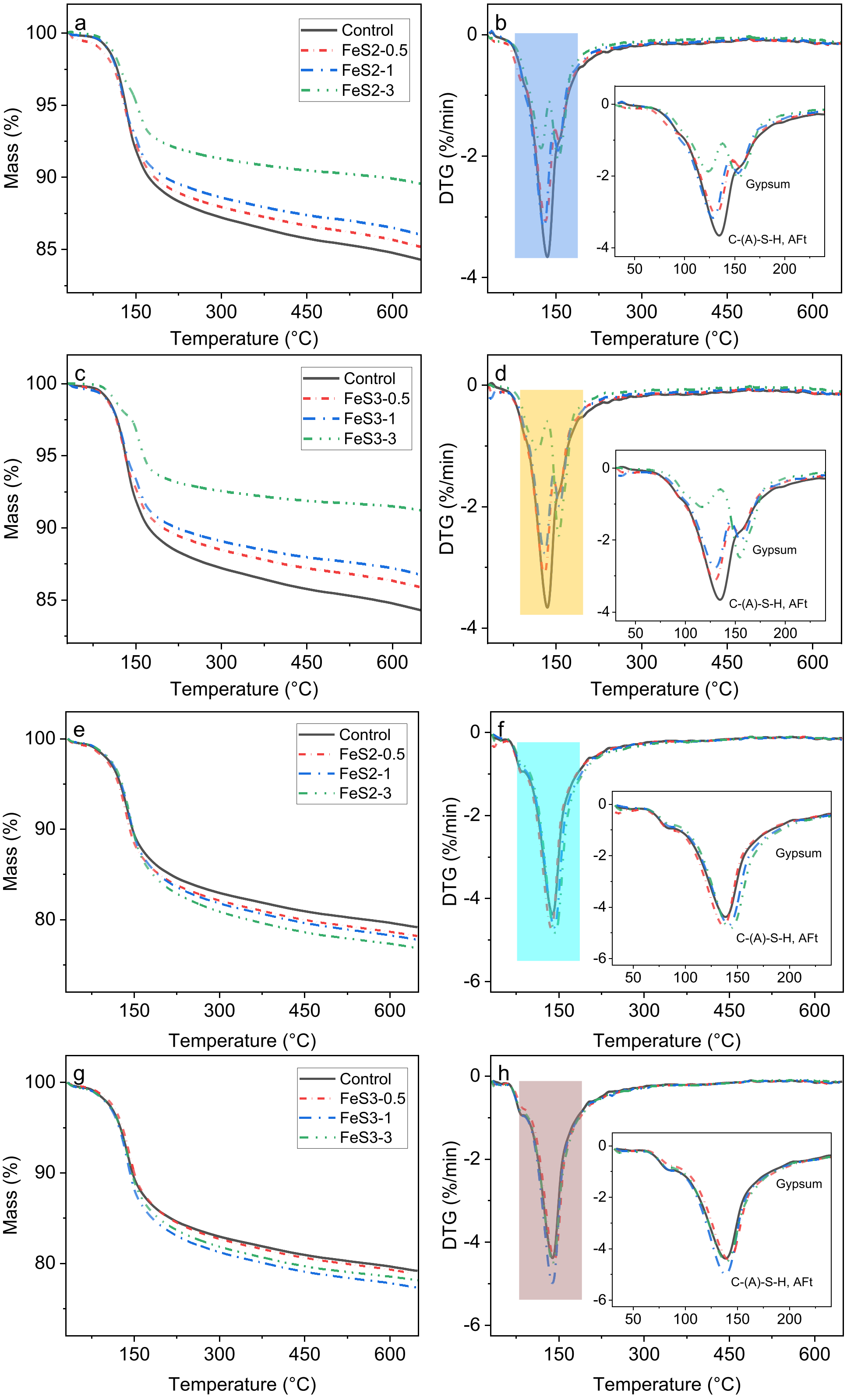

Fig. 10. TG analysis of the BAW samples after curing for 3d (a-d) and 28d (e-h).

compressive strength of BAW samples. Like FeS2/FeS3, the addition of FeC2/FeC3 inhibited the early compressive strength growth of BAW. At 0.5 wt%, 1 wt%, and 3 wt% FeC2, the 3d compressive strength of BAW decreased by about 8.56%, 21.95%, and 73.15%, respectively. Similarly, at 0.5 wt%, 1 wt%, and 3 wt% FeC3, the 3d compressive strength of BAW decreased by about 11.

$$2FeCl_3 + H_3AsO_4 + CaCO_3 + 2H_2O = Fe(OH)_3 + CaCl_2 + FeAsO_4 + 4HCl + CO_2\# \quad (10)$$

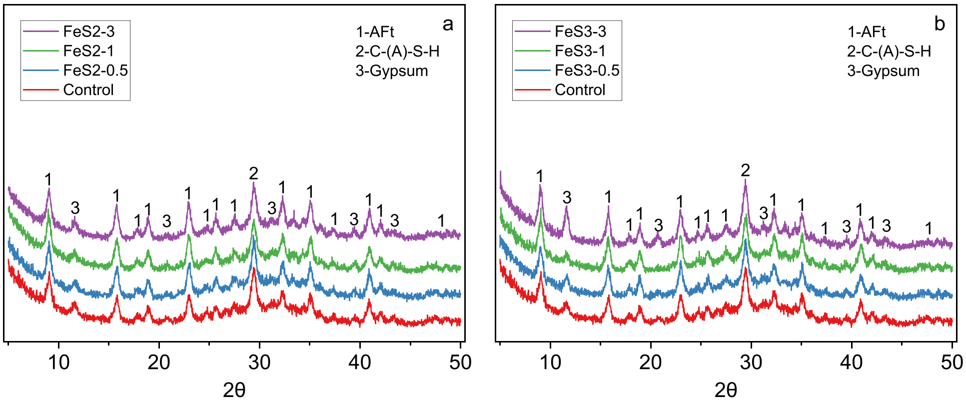

Fig. 11. XRD analysis of the BAW samples after curing for 28d: (a) FeS2, (b) FeS3.

3.4. *Reaction products*

Fig. 10 shows the results of TG analysis for the reaction products of BAW influenced by FeS2/FeS3 at 3d and 28d. According to Fig. 10a-d, at 3d, compared to the control sample, the addition of FeS2/FeS3 reduced the peak intensity at around 130 ℃ in the DTG curve, indicating a decrease in the production of C-(A)-S-H and ettringite. At the same time, the peak strength significantly increased at around 150 ℃, indicating an increase in the residual amount of gypsum. All of these phenomena indicate that the early reaction of BAW samples was inhibited, which limited the formation of reaction products and led to low early strength.

After curing for 28d, as the reaction proceeded, as shown in Fig. 10e-f, the peak intensity at around 130 ℃ increased compared to that at 3d, while the peak at around 150 ℃ disappeared, indicating that gypsum was exhausted, involved in the reaction, and generated more hydration products. In addition, after the addition of FeS2/FeS3, the peak strength at around 130 ℃ in the DTG curve slightly increased compared to the control sample, indicating that the addition of FeS2/FeS3 increased the generation of hydration products to a certain extent, which was consistent with the evolution of the compressive strength of the BAW sample at 28d. It is worth noting that when 3 wt% FeS3 was added, the amount of hydration products after curing for 28d was less than that of 1 wt% FeS3, as shown in Fig. 10h. This phenomenon was most likely due to the reaction in Eq. (10), which led to a low pH value of the entire reaction system. Even after long-term curing, the generation of hydration products was still inhibited.

Fig. 11 shows the XRD analysis of the reaction product after 28d affected by FeS2/FeS3. Similar to the results of TG analysis, the reaction products were mainly ettringite and C-(A)-S-H. The addition of FeS2/FeS3 did not change the phase composition of the reaction products. Additionally, the addition of FeS2/FeS3 led to an increase in peak intensity for ettringite, which could be attributed to the extra SO_4^{2-} favoring the formation of more ettringite. On the other hand, it can be seen from Fig. 11b that the intensity of the gypsum peak (11.6° 2θ) in sample FeS3–3 increased significantly, which was consistent with the TG results, indicating that the additional SO_4^{2-} introduced did not fully react.

The TG analysis results of FeC2/FeC3 on BAW reaction products were shown in Fig. 12. At 3d, the addition of FeC2/FeC3 inhibited the formation of reaction products to varying degrees, as indicated by the reduction of peak intensity around 130 ℃ in Fig. 12b and d. The inhibitory effect was enhanced with the increase in the dosage of FeC2/FeC3. At the same time, the peak strength at about 150 ℃ increased due to the incorporation of FeC2/FeC3, indicating an increase in the residual amount of gypsum. These results were consistent with the decreasing trend of compressive strength of the BAW samples.

After curing for 28d, the addition of FeC2/FeC3 had a less significant effect on the amount of reaction products than in the early stage, but the formation of hydration products was significantly inhibited when the dosage of FeC2/FeC3 reached 3 wt%. On the one hand, the reduction in the production of reaction products cannot provide sufficient chemical stability for As; on the other hand, it will increase the porosity of the sample and reduce the physical encapsulation effect of As. Thus, the increase in the dosage of FeC2/FeC3 resulted in a decrease in the immobilization rate of As due to the inhibition of reaction product formation.

Fig. 13 shows the XRD analysis of the reaction products after curing for 28d. In general, the incorporation of FeC2/FeC3 did not change the phase composition of the hydration products. However, samples with FeC2/FeC3 addition showed more residual gypsum. Since no additional SO_4^{2-} was introduced, the increase in the residual amount of gypsum also indirectly explained the inhibitory effect of FeC2/FeC3 on the BAW reaction.

3.5. *DFT calculation*

The addition of ferric/ferrous salt significantly improved the immobilization effect of As in BAW. On the one hand, it was due to the fact that the dissolved Fe species in the reaction system formed Fe-As complexes that were more stable than Ca-As and S-As complex [47–50], as shown in Eq. (15)~(14), thereby increasing the stability of As. Therefore, the surface complex of As species with FeOOH was investigated by DFT calculation.

$$4Fe^{3+} + 2AsO_4^{3-} + 6H_2O = 2FeAsO_4 + 2Fe(OH)_3 + 6H^+\# \tag{11}$$

$$4Fe^{2+} + 4H^+ + O_2 = 4Fe^{3+} + 2H_2O\# \tag{12}$$

$$Fe^{3+} + 3H_2O = Fe(OH)_3 + 3H^+\# \tag{13}$$

After 28 days of BAW reaction, the pH value of the pore solution was approximately 11 according to our previous work. As shown in Fig. S1, As in the pore solution mainly exists in the forms of $HAsO_4^{2-}$, AsO_4^{3-}, $HAsO_3^{2}$ and AsO_3^{3-}. However, in an alkaline environment, $HAsO_4^{2-}$ and $HAsO_3^{2-}$ easily lose protons to form AsO_4^{3-} and AsO_3^{3-} [51]. Therefore, the present work mainly focuses on AsO_4^{3-} (As(V)) and AsO_3^{3-} (As(III)).

3.5.1. *Stable adsorption configurations*

The surface of FeOOH (001) contains a large amount of unsaturated Fe, which can bind with O atoms in AsO_4^{3-}/AsO_3^{3-}. According to the number and configuration of shared O atoms between AsO_4^{3-}/AsO_3^{3-} and Fe atoms on the FeOOH (001) surface, the adsorption modes can be divided into monodentate complex (sharing one O atom) and bidentate complex (sharing two O atoms). The four adsorption configurations were geometrically optimized, and the results were shown in Fig. 14.

The configuration of AsO_4^{3-} on FeOOH (001) surface was shown in Fig. 14a and b. It can be seen that the adsorption energy of AsO_4^{3-} on the surface of FeOOH (001) was − 3.83 eV and − 4.30 eV by monodentate

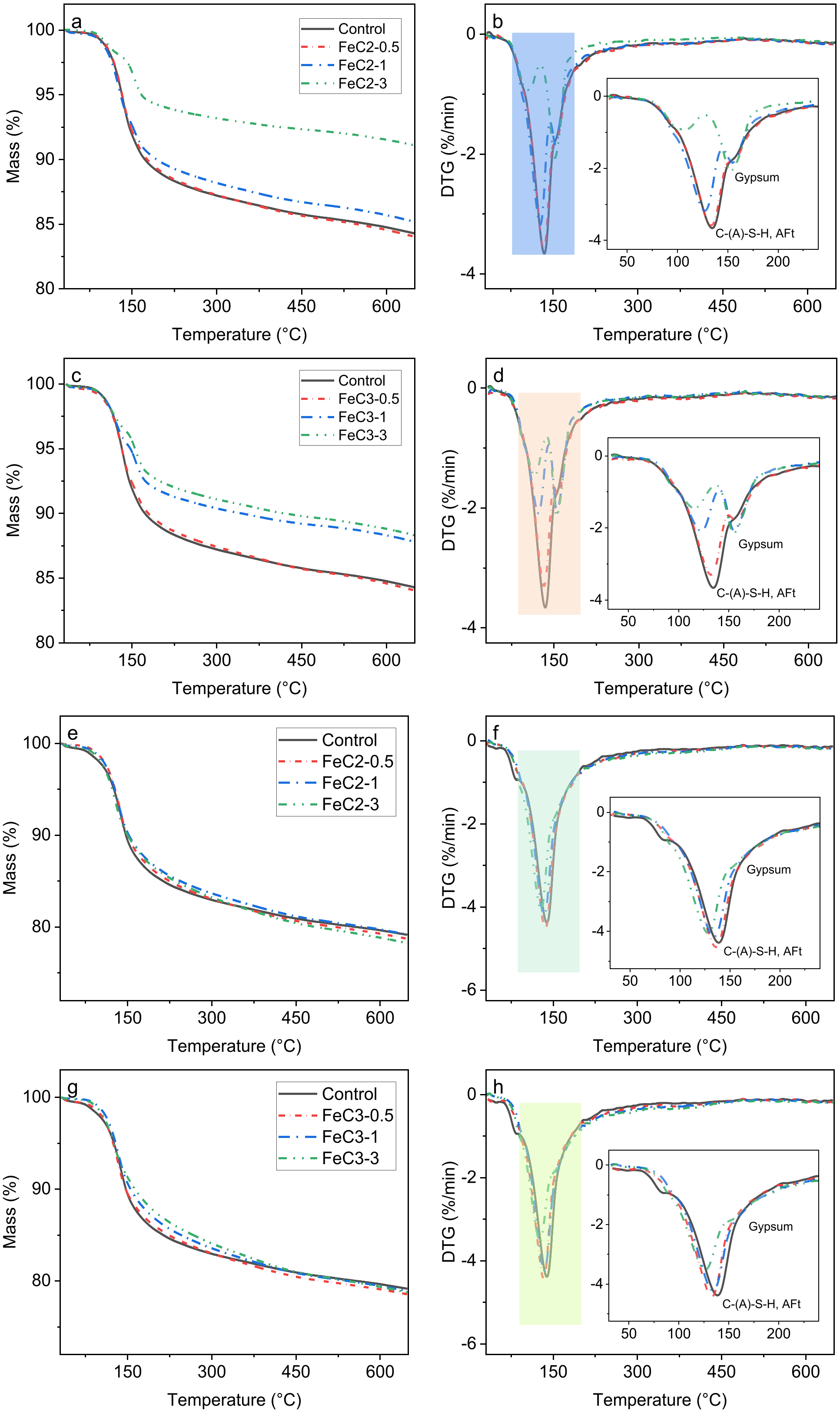

Fig. 12. TG analysis of the BAW samples: (a-d) FeC2, (e-f) FeC3.

and bidentate complex, respectively. Obviously, bidentate complex was more stable than monodentate complex. As shown in Fig. 14a, the distance between Fe10 and O65 (Fe10-O65) was 1.77 Å, and As-Fe10 was 3.64 Å, with the angle between As, O65 and Fe10 ($\angle_{\text{As-O65-Fe10}}$) being about 160.38°. For bidentate complex, the distance between Fe and O was larger, with Fe32-O66 and Fe24-O67 were about 1.85 Å and 1.86 Å, respectively. However, the smaller angle between As, O, and Fe resulted in a smaller distance between As and Fe, $\angle_{\text{As-O66-Fe32}} = 137.52°$, $\angle_{\text{As-O67-Fe24}} = 144.05°$, As-Fe24 and As-Fe32 were about 3.38 Å and 3.45 Å, respectively.

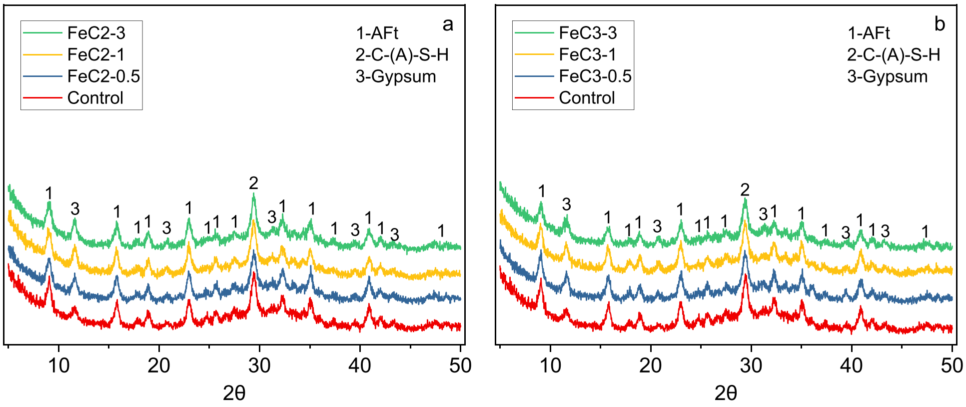

Fig. 13. XRD analysis of the BAW samples after curing for 28d: (a) FeC2, (b) FeC3.

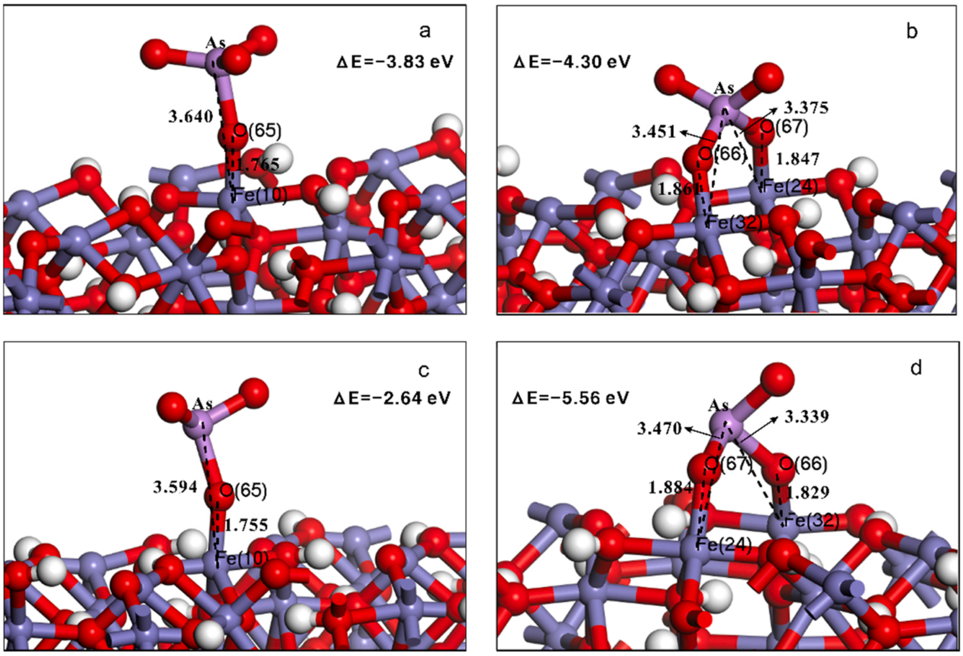

Fig. 14. Configurations of AsO_4^{3-} and AsO_3^{3-} after adsorbed onto the surface of FeOOH (001): (a) As(V)− 1, (b) As(V)− 2, (c) As(III)− 1, (d) As(III)− 2.

The configuration of AsO_3^{3-} on FeOOH (001) surface was shown in Fig. 14c and d, and the adsorption energies were − 2.64 eV and − 5.56 eV for monodentate complex and bidentate complex, respectively. For the adsorption through monodentate complex, Fe10-O65 and As-Fe10 were 1.76 Å and 3.59 Å, and $\angle_{As\text{-}O65\text{-}Fe10}$ = 156.13°. For bidentate complex, Fe24-O67 and As-Fe24 were 1.88 Å and 3.47 Å, $\angle_{As\text{-}O67\text{-}Fe24}$ = 132.57°; Fe32-O66 and As-Fe32 were 1.83 Å and 3.34 Å, $\angle_{As\text{-}O66\text{-}Fe32}$ = 142.56°.

The Mulliken's population can be used to describe the overlap of electrons between two atoms. The larger the population value, the stronger the covalency of the bond; conversely, the smaller the population value, the stronger the ionic property of the bond [52,53]. The larger the population absolute value, the stronger the interaction between the two orbitals. According to the results in Table S5, the population of Fe-O bond formed by O atoms in AsO_4^{3-} and AsO_3^{3-} and Fe atoms on FeOOH (001) surface was about 0.43–0.57, indicating the strong covalence.

Table S6 shows the changes in As-O bond length and population after the adsorption of AsO_4^{3-} and AsO_3^{3-} onto the FeOOH (001) surface. It can be observed from Table S6 that the population of As-O bonds interacting with Fe decreased significantly. This phenomenon is mainly attributed to the adsorption of O in AsO_4^{3-} and AsO_3^{3-} by unsaturated Fe atoms on the surface of FeOOH (001). Consequently, the bond length of As-O increased, and its covalency decreased. At the same time, bonding occurred between Fe and O atoms. Furthermore, the change in bond length and population of As-O was less significant in the bidentate complex than in the monodentate complex. This can be attributed to the ion binding effect of the As atom on the O in AsO_4^{3-} and AsO_3^{3-}.

3.5.2. *Density of states*

Density of states is used to represent the energy distribution of electrons in the reaction system and electronic properties [54–56]. Fig. 15 shows the partial density of states (PDOS) of AsO_3^{3-} before and after adsorption on FeOOH (001) surface. The PDOS of As atoms in AsO_3^{3-} between − 50 and − 20 eV was mainly contributed by the *d* orbital of As, and its peak value was relatively high, while PDOS between − 20 eV and 10 eV was contributed by the *s* and *p* orbitals of As (Fig. 15a). The PDOS of Fe atom traversed the Fermi level, indicating its high activity, and its PDOS at the Fermi level was mainly contributed by *d* orbitals (Fig. 15b and c). The PDOS of O atom between − 20 and − 10 eV was mainly contributed by *s* orbitals, while that between − 10 and 10 eV was mainly contributed by *p* orbitals (Fig. 15b and c).

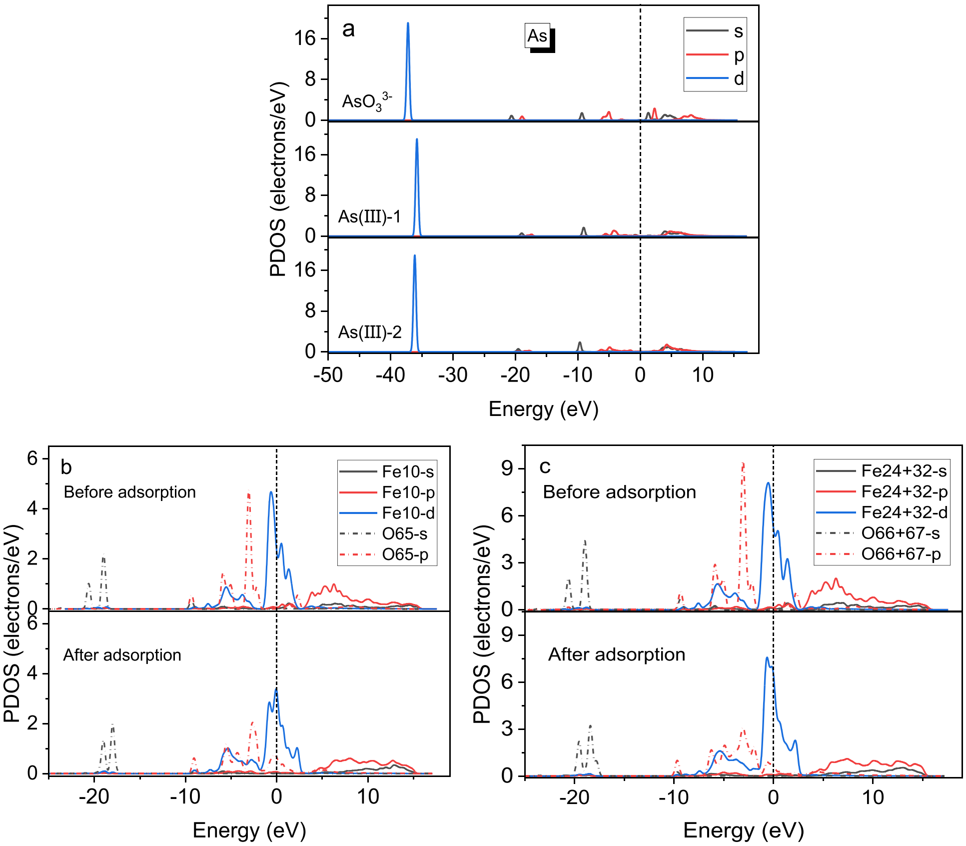

Fig. 15. Partial density of states before and after AsO_3^{3-} onto the FeOOH (001) surface.

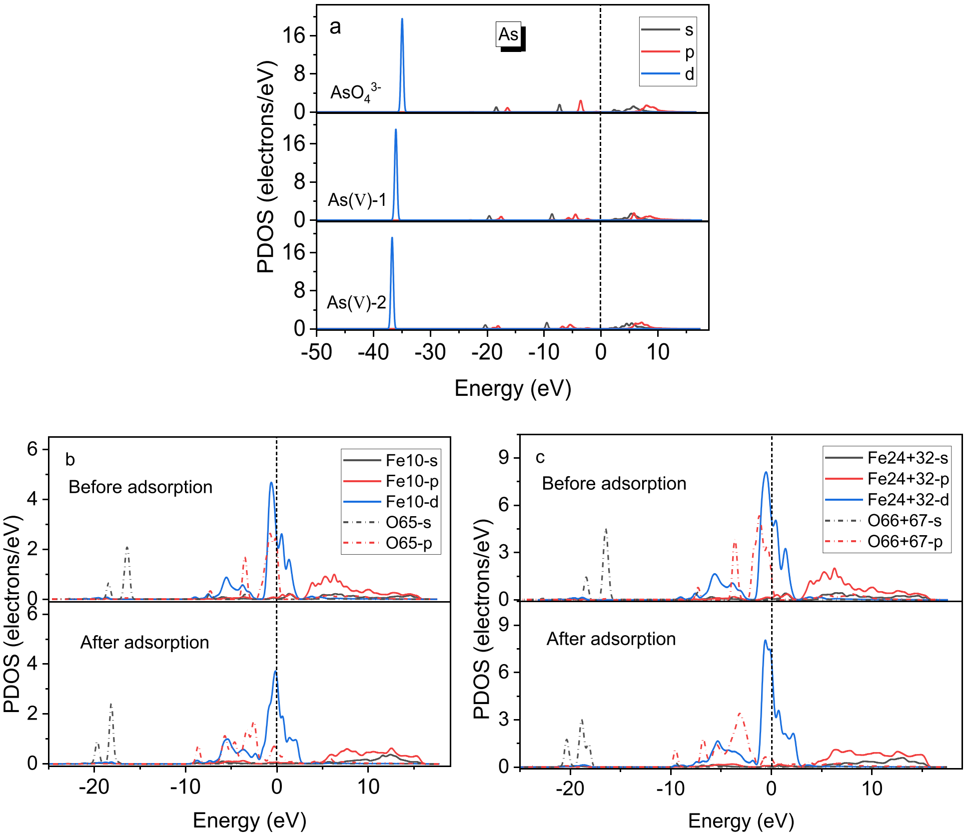

Fig. 16. Partial density of states before and after AsO_4^{3-} onto the FeOOH (001) surface.

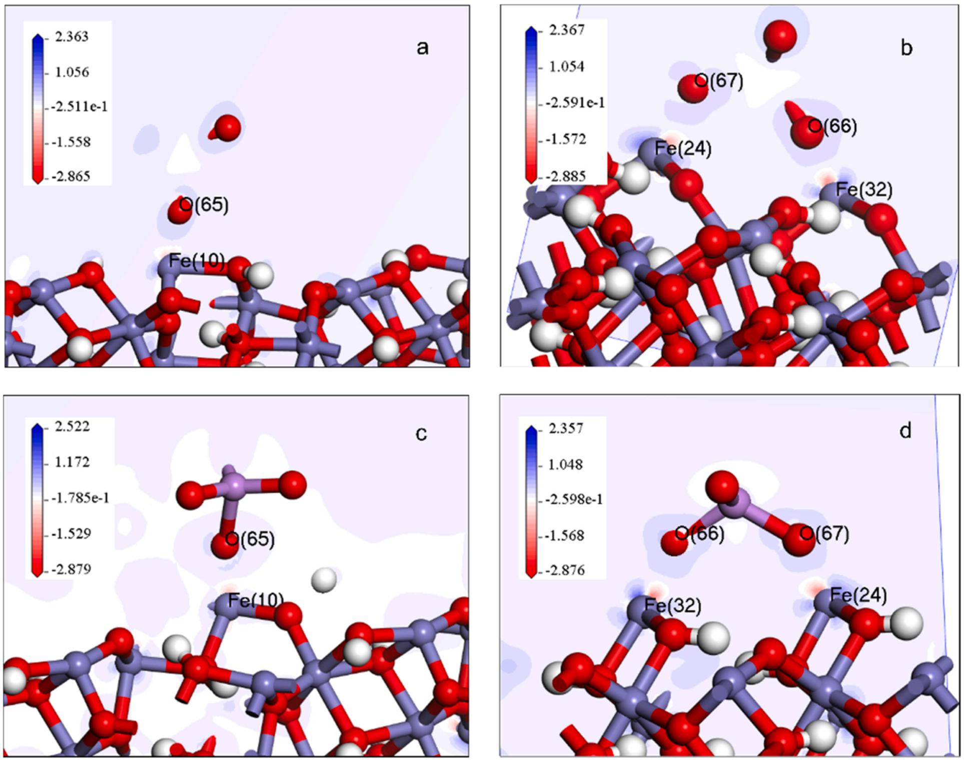

Fig. 17. The differential charge density after AsO_4^{3-} and AsO_3^{3-} adsorbed onto the FeOOH (001) surface: (a) As(III)− 1, (b) As(III)− 2, (c) As(V)− 1, (d) As(V)− 2.

From Fig. 15 b and c, it can be seen that the peak value of each orbital decreased to different degrees after the adsorption of As species. The d orbital of Fe and the *p* orbital of O overlapped between − 10 eV and 5 eV, indicating strong hybridization between them. This suggests that a chemical interaction occurred between Fe and O, leading to bond formation.

Fig. 16 shows the PDOS after AsO_4^{3-} adsorbed onto the FeOOH (001) surface. After adsorption of AsO_4^{3-} on the surface of FeOOH (001), it can be seen from Fig. 16a that the PDOS peak of As shifted towards the low energy direction, and the peak intensity of the *p* orbital near the Fermi level decreased significantly.

Additionally, it can be seen from Fig. 16b and c that the peak intensity of the PDOS of Fe and O also decreased to varying degrees, and the s and p orbitals of O both shifted towards the lower energy direction, indicating that the structure of AsO_4^{3-} became more stable after adsorption. On the other hand, similar to AsO_3^{3-}, the peaks of the d orbitals of Fe and the p orbitals of O overlap between − 10 and 5 eV, indicating strong hybridization and strong chemical interaction between them, which may lead to bond formation.

3.5.3. Differential charge density

Fig. 17 shows the differential charge density after the adsorption of AsO_4^{3-} and AsO_3^{3-} on the FeOOH (001) surface. The blue part in the picture indicates a gain of electrons, whereas the red part represents a loss of electrons. As depicted in Fig. 17, the differential charge density around the O atom was blue, indicating a significant electron enrichment around the surface, which is consistent with its strong electronegativity. In contrast, the red region near the Fe atom suggested that it had lost some electrons, which is related to the poor electronegativity of Fe and its weak binding ability to valence electrons. Therefore, it can be inferred that Fe and O atoms exhibit bonding effects.

4. Conclusions

The present work explored the feasibility of using ferric/ferrous salts to modify the As immobilization capacity of a binder prepared from AW through experiments and DFT calculations. Based on the results, the following conclusions can be drawn:

(1) The addition of ferric/ferrous salts strongly changed the chemical fractions of As, which was reflected in the significant decrease in the water-soluble fraction. This contributed to the reduction of As leaching from BAW samples.
(2) Among the four ferric/ferrous salts, FeS2 showed the best performance. Only 0.5 wt% FeS2 addition could achieve a high As immobilization rate of about 97.67%. However, higher amount of FeS2 did not favor a better immobilization effect resulting from the interfering with the binder reaction.
(3) The incorporation of ferric/ferrous salts decreased the early compressive strength of BAW, and the higher the dosage, the lower the early strength. Additionally, ferric salts had a more significant influence on the strength development than ferrous salts because they could lead to the formation of H_2SO_4 or HCl.
(4) AsO_4^{3-} and AsO_3^{3-} could be adsorbed onto the surface of FeOOH (001) via the formation of strong covalent bonds. Two adsorption modes, including monodentate complex and bidentate complex, could occur. The adsorption energies were about − 2.6~− 5.6 eV.

CRediT authorship contribution statement

Yingliang Zhao: Data curation, Writing – original draft preparation. **Yong Sun**: Visualization, Investigation. **Xiaogang Sun and Zhenbang Guo**: Supervision. **Jingping Qiu**: Conceptualization, Methodology.

Declaration of Competing Interest

The authors declare that they have no known competing financial interests or personal relationships that could have appeared to influence the work reported in this paper.

Data availability

Data will be made available on request.

Acknowledgment

The authors would like to thank the supports from National Natural Science Foundation of China (Key Program), 52234004.

Appendix A. Supporting information

Supplementary data associated with this article can be found in the online version at doi:10.1016/j.jece.2023.110206.

References

[1] D.-R. Zhang, J.-L. Xia, Z.-Y. Nie, H.-R. Chen, H.-C. Liu, Y. Deng, Y.-D. Zhao, L.-L. Zhang, W. Wen, H.-Y. Yang, Mechanism by which ferric iron promotes the bioleaching of arsenopyrite by the moderate thermophile Sulfobacillus thermosulfidooxidans, Process Biochem. 81 (2019) 11–21.

[2] A.H. Kaksonen, X. Deng, T. Bohu, L. Zea, H.N. Khaleque, Y. Gumulya, N.J. Boxall, C. Morris, K.Y. Cheng, Prospective directions for biohydrometallurgy, Hydrometallurgy 195 (2020), 105376.

[3] D. Langhans, A. Lord, D. Lampshire, A. Burbank, E. Baglin, Biooxidation of an arsenic-bearing refractory gold ore, Miner. Eng. 8 (1995) 147–158.

[4] J.A. Brierley, Response of microbial systems to thermal stress in biooxidation-heap pretreatment of refractory gold ores, Hydrometallurgy 71 (2003) 13–19.

[5] M.E.L. Arrascue, J. van Niekerk, Biooxidation of arsenopyrite concentrate using BIOX® process: Industrial experience in Tamboraque, Peru, Hydrometallurgy 83 (2006) 90–96.

[6] H. Tao, L. Dongwei, Presentation on mechanisms and applications of chalcopyrite and pyrite bioleaching in biohydrometallurgy - a presentation, Biotechnol. Rep. 4 (2014) 107–119.

[7] Y. Li, X. Zhu, X. Qi, B. Shu, X. Zhang, K. Li, Y. Wei, H. Wang, Removal and immobilization of arsenic from copper smelting wastewater using copper slag by in situ encapsulation with silica gel, Chem. Eng. J. 394 (2020), 124833.

[8] Y. Miao, S. Qi, G. Chen, X. Wang, W. Zhao, J. Wang, S. Zhang, B. Xin, Efficient removal of As, Cu and Cd and synthesis of photo-catalyst from Cu-smelting waste acid through sulfide precipitation by biogenic gaseous H_2S produced by anaerobic membrane bioreactor, Chem. Eng. J. 451 (2023), 138096.

[9] X. Duan, X. Li, Y. Li, X. Qi, G. Li, Z. Lu, N. Yang, Separation and stabilization of arsenic in copper smelting wastewater by zinc slag, J. Clean. Prod. 312 (2021), 127797.

[10] X. Sun, J. Li, X. Sun, J. Zheng, Z. Wu, W. Liu, D. Zhao, Z. Lin, Efficient stabilization of arsenic in the arsenic-bearing lime-ferrate sludge by zero valent iron-enhanced hydrothermal treatment, Chem. Eng. J. 421 (2021), 129683.

[11] B. Peng, J. Lei, X.-B. Min, L.-Y. Chai, Y.-J. Liang, Y. You, Physicochemical properties of arsenic-bearing lime–ferrate sludge and its leaching behaviors, Trans. Nonferrous Met. Soc. China 27 (2017) 1188–1198.

[12] L. Guo, Y. Du, Q. Yi, D. Li, L. Cao, D. Du, Efficient removal of arsenic from “dirty acid” wastewater by using a novel immersed multi-start distributor for sulphide feeding, Sep. Purif. Technol. 142 (2015) 209–214.

[13] F. Lagno, S.D.F. Rocha, S. Chryssoulis, G.P. Demopoulos, Scorodite encapsulation by controlled deposition of aluminum phosphate coatings, J. Hazard. Mater. 181 (2010) 526–534.

[14] Y. Li, Y. Xu, X. Zhu, H. Wang, X. Qi, K. Li, Y. Wei, Sodification/stabilization of arsenic-bearing gypsum sludge using Portland cement: precalcination effect and arsenic immobilization mechanism, Chin. J. Process Eng. 18 (2018) 111–121.

[15] H. Xu, X. Min, Y. Wang, Y. Ke, L. Yao, D. Liu, L. Chai, Stabilization of arsenic sulfide sludge by hydrothermal treatment, Hydrometallurgy 191 (2020), 105229.

[16] D. Yang, A. Sasaki, M. Endo, Reclamation of an arsenic-bearing gypsum via acid washing and CaO-As stabilization involving svabite formation in thermal treatment, J. Environ. Manag. 231 (2019) 811–818.

[17] D. Yang, A. Sasaki, M. Endo, Reclamation of a waste arsenic-bearing gypsum as a soil conditioner via acid treatment and subsequent Fe(II) As stabilization, J. Clean. Prod. 217 (2019) 22–31.

[18] V.R. Ouhadi, R.N. Yong, M. Deiranlou, Enhancement of cement-based solidification/stabilization of a lead-contaminated smectite clay, J. Hazard. Mater. 403 (2021), 123969.

[19] Y.-S. Feng, Y.-J. Du, A. Zhou, M. Zhang, J.-S. Li, S.-J. Zhou, W.-Y. Xia, Geoenvironmental properties of industrially contaminated site soil solidified/stabilized with a sustainable by-product-based binder, Sci. Total Environ. (2020), 142778.

[20] A. Bah, J. Jin, A.O. Ramos, Y. Bao, M. Ma, F. Li, Arsenic(V) immobilization in fly ash and mine tailing-based geopolymers: Performance and mechanism insight, Chemosphere 306 (2022), 135636.

[21] Q. Tian, C. Chen, M. Wang, B. Guo, H. Zhang, K. Sasaki, Effect of Si/Al molar ratio on the immobilization of selenium and arsenic oxyanions in geopolymer, Environ. Pollut. 274 (2021), 116509.

[22] V.P. Mehrotra, A. Sai, P.C. Kapur, Plaster of Paris activated supersulfated slag cement, Cem. Concr. Res. 12 (1982) 463–473.

[23] Y. Zhao, X. Gu, J. Qiu, S. Zhang, Z. Guo, X. Sun, Recycling of arsenic-containing biohydrometallurgy waste to produce a binder for cemented paste backfill: Co-treatment with oil shale residue, J. Environ. Manag. 319 (2022), 115621.

[24] Y. Zhao, X. Gu, J. Qiu, S. Zhang, Z. Guo, X. Sun, Recycling of arsenic-containing biohydrometallurgy waste to produce a binder for cemented paste backfill: Influence of additives, J. Clean. Prod. (2022), 132515.

[25] Y. Zhao, J. Qiu, S. Zhang, Z. Guo, P. Wu, X. Sun, X. Gu, Recycling of arsenic-containing biohydrometallurgy waste to produce a binder for cemented paste backfill: Mix proportion optimization, Powder Technol. 398 (2022), 117155.

[26] B. Guo, B. Liu, J. Yang, S. Zhang, The mechanisms of heavy metal immobilization by cementitious material treatments and thermal treatments: A review, J. Environ. Manag. 193 (2017) 410–422.

[27] M. Chrysochoou, D. Dermatas, Evaluation of ettringite and hydrocalumite formation for heavy metal immobilization: literature review and experimental study, J. Hazard. Mater. 136 (2006) 20–33.

[28] D. Wang, Q. Wang, Clarifying and quantifying the immobilization capacity of cement pastes on heavy metals, Cem. Concr. Res. 161 (2022), 106945.

[29] M. Zhang, C. Yang, M. Zhao, L. Yu, K. Yang, X. Zhu, X. Jiang, Immobilization of Cr (VI) by hydrated Portland cement pastes with and without calcium sulfate, J. Hazard. Mater. 342 (2018) 242–251.

[30] L. Liu, Z.H. Yang, L.Y. Chai, Y.P. Liao, W.B. Yao, Z. Zhang, Y. Liu, Stabilization of As in soil using two kinds of Fe(III) salts, AMM 768 (2015) 142–149.

[31] W.G. Cutler, A. El-Kadi, N.V. Hue, J. Peard, K. Scheckel, C. Ray, Iron amendments to reduce bioaccessible arsenic, J. Hazard. Mater. 279 (2014) 554–561.

[32] X. Wang, H. Zhang, L. Wang, J. Chen, S. Xu, H. Hou, Y. Shi, J. Zhang, M. Ma, D.C. W. Tsang, J.C. Crittenden, Transformation of arsenic during realgar tailings stabilization using ferrous sulfate in a pilot-scale treatment, The, Sci. Total Environ. 668 (2019) 32–39.

[33] L.-F. Hu, H.-J. Feng, Y.-Y. Wu, Y.-Y. Long, J. Wang, D.-S. Shen, A comparative study on stabilization of available As in highly contaminated hazardous solid waste, J. Hazard. Mater. 174 (2010) 194–201.

[34] X. Wang, J. Ding, L. Wang, S. Zhang, H. Hou, J. Zhang, J. Chen, M. Ma, D.C. Tsang, X. Wu, Stabilization treatment of arsenic-alkali residue (AAR): Effect of the coexisting soluble carbonate on arsenic stabilization, Environ. Int. 135 (2020), 105406.

[35] Y. Liang, X. Min, L. Chai, M. Wang, W. Liyang, Q. Pan, M. Okido, Stabilization of arsenic sludge with mechanochemically modified zero valent iron, Chemosphere 168 (2017) 1142–1151.

[36] Y. Songrong, Fundamental and Industrialization Investigation on Biooxidation of Arsenic-bearing Refractory Gold Ore. Chinese Doctoral Dissertations, 2004.

[37] K. Irisawa, M. Namiki, T. Taniguchi, I. Garcia-Lodeiro, H. Kinoshita, Solidification and stabilization of strontium and chloride ions in thermally treated calcium aluminate cement modified with or without sodium polyphosphate, Cem. Concr. Res. 156 (2022), 106758.

[38] Y. Zhang, W. Gao, W. Ni, S. Zhang, Y. Li, K. Wang, X. Huang, P. Fu, W. Hu, Influence of calcium hydroxide addition on arsenic leaching and solidification/stabilisation behaviour of metallurgical-slag-based green mining fill, J. Hazard. Mater. 390 (2020), 122161.

[39] R. Snellings, J. Chwast, Ö. Cizer, N. de Belie, Y. Dhandapani, P. Durdzinski, J. Elsen, J. Haufe, D. Hooton, C. Patapy, M. Santhanam, K. Scrivener, D. Snoeck, L. Steger, S. Tongbo, A. Vollpracht, F. Winnefeld, B. Lothenbach, Report of TC 238-SCM: hydration stoppage methods for phase assemblage studies of blended cements—results of a round robin test, Mater. Struct. 51 (2018) 1.

[40] X. Chen, A. Meawad, L.J. Struble, Method to stop geopolymer reaction, J. Am. Ceram. Soc. 97 (2014) 3270–3275.

[41] J. Zhang, G.W. Scherer, Comparison of methods for arresting hydration of cement, Cem. Concr. Res. 41 (2011) 1024–1036.

[42] H. Zhang, W. Sun, Y. Zhu, J. He, D. Chen, C. Zhang, Effects of the goethite surface hydration microstructure on the adsorption of the collectors dodecylamine and sodium oleate, Langmuir ACS J. Surf. Colloids 37 (2021) 10052–10060.

[43] A. Fernández-Martínez, G.J. Cuello, M.R. Johnson, F. Bardelli, G. Román-Ross, L. Charlet, X. Turrillas, Arsenate incorporation in gypsum probed by neutron, X-ray scattering and density functional theory modeling, J. Phys. Chem. A 112 (2008) 5159–5166.

[44] Vanderbilt, Soft self-consistent pseudopotentials in a generalized eigenvalue formalism, Phys. Rev. B 41 (1990) 7892–7895.

[45] Y. Liang, Y. Liao, L. Kang, Z. Lin, J. Ma, F. Zhao, J. Song, Y. Ke, X. Min, C. Peng, Stabilization of ferric arsenate sludge with ZVI intensive corrosion and enhancement of long-term arsenic immobilization via resin encapsulation, J. Environ. Chem. Eng. 10 (2022), 107392.

[46] J.-Y. Kim, A.P. Davis, K.-W. Kim, Stabilization of available arsenic in highly contaminated mine tailings using iron, Environ. Sci. Technol. 37 (2003) 189–195.

[47] P.M. Randall, Arsenic encapsulation using Portland cement with ferrous sulfate/lime and Terra-Bond™ technologies - Microcharacterization and leaching studies, Sci. Total Environ. 420 (2012) 300–312.

[48] E. Li, T. Yang, Q. Wang, Z. Yu, S. Tian, X. Wang, Long-term stability of arsenic calcium residue (ACR) treated with $FeSO_4$ and H_2SO_4: Function of H^+ and Fe(II), J. Hazard. Mater. 420 (2021), 126549.

[49] Q. Shi, G.E. Sterbinsky, S. Zhang, C. Christodoulatos, G.P. Korfiatis, X. Meng, Formation of Fe(iii)–As(v) complexes: effect on the solubility of ferric hydroxide precipitates and molecular structural identification, Environ. Sci.: Nano 7 (2020) 1388–1398.

[50] P. Miretzky, A.F. Cirelli, Remediation of arsenic-contaminated soils by iron amendments: a review, Crit. Rev. Environ. Sci. Technol. 40 (2010) 93–115.

[51] Gonçalves Jr Paulo Roberto Garcês, H.A. de Abreu, H.A. Duarte, Arsenic adsorption on Mn3O4 surface: As(OH)3/AsO(OH)3 oxidation mechanism, Appl. Surf. Sci. 580 (2022), 152213.

[52] B. Ren, F. Min, J. Chen, F. Fang, C. Liu, Adsorption mechanism insights into CPAM structural units on kaolinite surfaces: A DFT simulation, Appl. Clay Sci. 197 (2020), 105719.

[53] B. Ren, F. Min, L. Liu, J. Chen, C. Liu, K. Lv, Adsorption of different PAM structural units on kaolinite (0 0 1) surface: Density functional theory study, Appl. Surf. Sci. 504 (2020), 144324.

[54] S. Qiu, H. Wu, H. Yan, X. Li, X. Zhou, T. Qiu, Theoretical investigation of hydrated [Lu(OH)2]+ adsorption on kaolinite(0 0 1) surface with DFT calculations, Appl. Surf. Sci. 565 (2021), 150473.

[55] T. Qiu, S. Qiu, H. Wu, H. Yan, X. Li, X. Zhou, Adsorption of hydrated [Y(OH)2]+ on kaolinite (001) surface: Insight from DFT simulation, Powder Technol. 387 (2021) 80–87.

[56] B. Dash, S.S. Rath, Density Functional Theory and Molecular Dynamics insights into the site-dependent adsorption of hydrogen fluoride on kaolinite, J. Mol. Liq. 299 (2020), 112265.